A Scale-Adaptive Turbulent Kinetic Energy Closure for the Dry Convective Boundary Layer

MARCIN J. KUROWSKI AND JOÃO TEIXEIRA

Jet Propulsion Laboratory, California Institute of Technology, Pasadena, and Joint Institute for Regional Earth System Science and Engineering, University of California, Los Angeles, Los Angeles, California

(Manuscript received 19 October 2016, in final form 28 November 2017)

ABSTRACT

A pragmatic scale-adaptive turbulent kinetic energy (TKE) closure is proposed to simulate the dry convective boundary layer for a variety of horizontal grid resolutions: from 50 m, typical of large-eddy simulation models that use three-dimensional turbulence parameterizations/closures, up to 100 km, typical of climate models that use one-dimensional turbulence and convection parameterizations/closures. Since parameterizations/closures using the TKE approach have been frequently used in these two asymptotic limits, a simple method is proposed to merge them with a mixing-length-scale formulation for intermediate resolutions. This new scale-adaptive mixing length naturally increases with increasing grid length until it saturates as the grid length reaches mesoscale-model resolution. The results obtained using this new approach for dry convective boundary layers are promising. The mean vertical profiles of potential temperature and heat flux remain in good agreement for different resolutions. A continuous transition (in terms of resolution) across the gray zone is illustrated through the partitioning between the model-resolved and the subgrid-scale transports as well as by documenting the transition of the subgrid-scale TKE source/sink terms. In summary, a natural and continuous transition across resolutions (from 50 m to 100 km) is obtained, for dry convection, using exactly the same atmospheric model for all resolutions with a simple scale-adaptive mixing-length formulation.

1. Introduction

The turbulent gray-zone problem appears as one of the most challenging issues in atmospheric boundary layer modeling. It was elaborated in detail by Wyngaard (2004) and is associated with the transition from fully three-dimensional subgrid-scale (SGS) turbulence, characteristic of small-scale models such as large-eddy simulation (LES) models, to a one-dimensional (1D) SGS representation characteristic of coarse-resolution weather and climate models. In 2005, a workshop on the parameterization of the atmospheric boundary layer (Teixeira et al. 2008) concluded that it is currently unclear what the adequate boundary layer parameterizations are for horizontal resolutions on the order of 1 km; that, at these horizontal resolutions, the 1D approach is no longer fully adequate; and that parameterizations should contain information about the horizontal resolution in their formulation to allow for smooth transitions between different resolutions. For the high-resolution limit, the turbulence within a grid box is assumed isotropic and often constitutes a residual part of the resolved turbulent transport. For the coarse-resolution limit, however, the filtered equations of motion primarily describe the large-scale flow, and the SGS turbulent transport plays a key role in the vertical distribution of heat, moisture, and momentum.

There are a few important questions associated with the transition between these two asymptotic limits. One is how to realistically represent the unresolved part of the turbulent transport with fully three-dimensional schemes for an increasing model grid length (i.e., bottom-up approach), which can reach beyond the inertial subrange of turbulence. This leads to the question of how the originally coarse-resolution one-dimensional boundary layer parameterizations should respond to a refined grid length in a physically sound manner (i.e., top-down approach). The top-down approach adds more complexity to this transition as it involves the issues related with the moist convection gray zone that extends far beyond the turbulent gray zone (e.g., Holloway et al. 2014; Fan et al. 2015).

Corresponding author: Marcin J. Kurowski, marcin.j.kurowski@jpl.nasa.gov

DOI: 10.1175/JAS-D-16-0296.1

Honnert et al. (2011) analyzed features of the gray-zone transition for the dry convective boundary layer by applying a coarse-graining method to LES results. It allowed for a formal quantification of the partitioning between the model-resolved and the subgrid-scale transports of temperature, moisture, and turbulent kinetic energy as a function of filter scale. Using the same methodology, Shin and Hong (2013) extended this analysis to a forced convection case. They further investigated the partitioning between the nonlocal and local transports within the gray zone (Shin and Hong 2015). All the results suggested that the vertical SGS transport should be continuously downweighted while refining the resolution within the nonhydrostatic regime to allow for an equitable representation of the resolved part of kinetic energy. However, such a decrease in SGS transport depends on the simulated case and is somewhat different for different model variables. It may also vary with the z/z_i ratio, where z_i is the height of the boundary layer. Another conclusion from Shin and Hong (2015) was that the inclusion of a nonlocal mass-flux term in a scale-dependent parameterization could be more important than an adjustment of the eddy-diffusivity local term. It appears that the key role of the nonlocal scheme is to counteract a systematic underestimation of the vertical mixing by conventional local schemes at coarser resolutions (Takemi and Rotunno 2003; Cheng et al. 2010; Honnert et al. 2011; LeMone et al. 2013; Shin and Hong 2015).

Based on these findings, Shin and Hong (2015) employed a resolution-dependent suppression of the 1D SGS fluxes derived by the boundary layer scheme to simulate a set of idealized buoyancy- and shear-driven convective cases (for grid lengths of 1 km, 500 m, and 250 m) as well as a real case of convective rolls (for grid lengths of 1 km and 333 m). They showed that the approach not only makes it possible to simulate consistent evolutions of mean temperature profiles at different resolutions but also helps to preserve similar statistics of the model-resolved kinetic energy.

A somewhat different idea was proposed by Boutle et al. (2014) to improve a real-case simulation of a stratocumulus-topped boundary layer for model grid lengths of 1 km and 333 and 100 m. By using a scale-dependent function for turbulent kinetic energy (TKE) from Honnert et al. (2011), they blended a nonlocal boundary layer parameterization with a Smagorinsky-type turbulence scheme. In this approach, the one-dimensional SGS transport decreases with decreasing model grid length in a similar way as in the Shin and Hong (2015) experiment. At the same time, the three-dimensional local scheme becomes increasingly important at higher resolutions and eventually dominates in the LES regime. This interesting idea deserves a more detailed investigation since the transition from 3D to 1D turbulence (cf. Honnert et al. 2011) and the horizontal (physical and numerical) transport may have different scale-dependent characteristics (Shin and Hong 2015). It is worth mentioning that the recent works of Dorrestijn et al. (2013), Zhou et al. (2014), Ito et al. (2015), Efstathiou and Beare (2015), Kitamura (2016), Bhattacharya and Stevens (2016), and Honnert (2016) also contributed to the overall effort of developing scale-adaptive turbulence parameterizations.

In this study, we explore the potential for scale adaptivity of a local SGS transport scheme across the full range of resolutions employed by atmospheric models. First, we make the simple observation that local SGS closures based on the prognostic TKE equation have been widely used both in the small-scale (3D) and the large-scale (1D) limits. Therefore, we exclusively focus on this closure and adapt it to intermediate resolutions by changing the mixing-length formulation using a method inspired by how Blackadar (1962) blended the surface layer with the well-mixed boundary layer above. Note that the formulation being proposed fits the unified closure concept from Wyngaard (2004). The scale dependence is achieved intrinsically without using any external functions to prescribe the partitioning between the SGS and resolved transports [as is done, for example, in Boutle et al. (2014), who use an explicit blending function]. We then examine the proposed approach for horizontal grid lengths ranging from 50 m up to 100 km for a set of idealized dry convection simulations.

This paper is organized as follows. Section 2 describes the methodology of the proposed approach. In section 3, we present the numerical experiment, which we use to test our approach in section 4. Summary and conclusions are provided in section 5.

2. Methodology

A key element of the analysis is the spatial filtering of each model variable f represented on a discretized grid. It is formally defined as

$$\overline{f}(\mathbf{x},t)=\frac{1}{V}\int_V f(\mathbf{x}+\mathbf{x}',t)\,d\mathbf{x}', \tag{1}$$

where $V=\Delta x\Delta y\Delta z$ is the volume of a grid box, with Δi denoting the grid length in the ith direction and $\mathbf{x}+\mathbf{x}'$ the location within the grid box. We apply this filter to the model equations using a range of filter scales.

a. The SGS model

For decomposed model variables, $f=\overline{f}+f'$, the filtered part is explicitly resolved, whereas the unresolved part contributes to the SGS transport in the

form of the $\overline{f'u_i'}$ fluxes. It is commonly assumed that they can be represented through the resolved variables as

$$\overline{f'u_i'} = -K_f \frac{\partial \overline{f}}{\partial x_i}, \tag{2}$$

with K_f denoting the turbulent transport coefficient for f. To represent the SGS fluxes, we employ the scheme based on turbulent kinetic energy (Deardorff 1980). For this approach, the turbulent eddy viscosity coefficient for momentum within a grid box is defined as

$$K_m = C_k l e^{1/2}, \tag{3}$$

where C_k is a constant; l the mixing length; $e = 0.5(\overline{u'u'} + \overline{v'v'} + \overline{w'w'})$ the turbulent kinetic energy; and u, v, and w denote the three components of velocity.

The eddy-diffusivity coefficient for heat and TKE has the form

$$K_h = \frac{K_m}{\mathrm{Pr}}, \tag{4}$$

where Pr is the turbulent Prandtl number. In this study, we use the same turbulent transport coefficients in the horizontal and vertical. However, horizontal transport becomes negligible for larger grid lengths because of diminishing mean horizontal gradients of the transported fields. Note that the coarse-resolution weather forecasting models frequently use additional numerical filtering to smooth out the horizontal fields while using a one-dimensional boundary layer parameterization. In this context, such filtering can be applied through the appropriately modified mixing coefficients of the horizontal diffusion (e.g., Skamarock et al. 2008).

b. Turbulent kinetic energy

We start with a theoretical consideration of the behavior of the kinetic energy closure for the small- and large-scale limits. The prognostic equation for the SGS turbulent kinetic energy takes the general form

$$\frac{\partial e}{\partial t} = A + S + B + T + D, \tag{5}$$

where A, S, B, and T represent, respectively, the advection, shear production, buoyancy production, and transport terms and D is the energy dissipation rate. The right-hand-side sink/source terms in Eq. (5) for the small-scale (3D) limit are defined as

$$A = -\left(\overline{u}\frac{\partial e}{\partial x} + \overline{v}\frac{\partial e}{\partial y} + \overline{w}\frac{\partial e}{\partial z}\right), \tag{6}$$

$$S = -\left(\overline{u'u'}\frac{\partial \overline{u}}{\partial x} + \overline{v'u'}\frac{\partial \overline{u}}{\partial y} + \overline{w'u'}\frac{\partial \overline{u}}{\partial z} + \overline{u'v'}\frac{\partial \overline{v}}{\partial x} + \overline{v'v'}\frac{\partial \overline{v}}{\partial y} + \overline{w'v'}\frac{\partial \overline{v}}{\partial z} + \overline{u'w'}\frac{\partial \overline{w}}{\partial x} + \overline{v'w'}\frac{\partial \overline{w}}{\partial y} + \overline{w'w'}\frac{\partial \overline{w}}{\partial z}\right), \tag{7}$$

$$B = \frac{g}{\overline{\theta}}\overline{w'\theta'}, \tag{8}$$

$$T = -\left[\frac{\partial(\overline{u'e'} + \overline{u'p'})}{\partial x} + \frac{\partial(\overline{v'e'} + \overline{v'p'})}{\partial y} + \frac{\partial(\overline{w'e'} + \overline{w'p'})}{\partial z}\right], \tag{9}$$

and

$$D = -\frac{C_\epsilon e^{3/2}}{l_\epsilon}, \tag{10}$$

where g is the gravitational constant, θ the potential temperature, p the density-weighted pressure, C_ϵ is a constant, and l_ϵ defines the length scale associated with the dissipation of TKE (typically $l_\epsilon = l$).

For the large-scale filter limit (i.e., for $\Delta x, \Delta y \to L$, where L is on the order of 10 km), in the absence of external flow ($\overline{u} = 0$, $\overline{v} = 0$), the mean flow within a grid box diminishes, and the resolved part becomes horizontally homogeneous (i.e., $\partial/\partial x = 0$, $\partial/\partial y = 0$; also, $\overline{w} = 0$). Equations (6)–(9) can be then approximated by

$$A = 0, \tag{11}$$

$$S = 0, \tag{12}$$

$$B = \frac{g}{\overline{\theta}}\overline{w'\theta'}, \tag{13}$$

$$T = -\frac{\partial(\overline{w'e'} + \overline{w'p'})}{\partial z} \tag{14}$$

which yields a one-dimensional form characteristic of a single-column model representation (cf. Witek et al. 2011b). The pressure work terms in T are typically neglected, while the turbulent transport of TKE is parameterized using the flux–gradient method [cf. Skamarock et al. (2008) for the model used in this study; see section 3], with the transport coefficient $K_e = K_h$. For the above transition between the 3D and 1D limits, one can expect the small-scale terms A and S to decrease with increasing grid length and the B and T terms to increase at the cost of the model-resolved transport. Note that, although B has formally the same definitions in Eqs. (8) and (13), their meanings are significantly different since they account for residual or entire vertical transport, respectively. This is also the case for the remaining terms in T.

A potential versatility of the TKE closure lies in its natural scale-adaptive behavior, with the appropriate SGS terms likely changing with the filter scale. One clear disadvantage is that the diffusivity term in the model equations is a scalar field because of the assumption of isotropic turbulence within a grid box. This issue can be to some degree improved by using separate mixing coefficients in the horizontal and vertical, as mentioned earlier. Knowing the limits of the TKE scheme, our main goal is to examine whether its adjustment across commonly used grid lengths is feasible and what the accuracy of such an approach is.

c. *Scale-adaptive mixing-length formulation*

We propose a new formulation for the mixing length that can be applied to a range of model grid lengths. It continuously merges the fine- and coarse-resolution limits that we recall below.

For the small-scale (3D) limit, the mixing length is based on the geometric properties of the grid box; for example (Deardorff 1980),

$$l_{3D} = (\Delta x \Delta y \Delta z)^{1/3}. \tag{15}$$

This definition is scale aware yet has no upper limit.

For the large-scale (1D) limit, the mixing length usually depends on some fundamental properties of the boundary layer (e.g., Mellor and Yamada 1974; Grenier and Bretherton 2001; Teixeira and Cheinet 2004). For the reasons explained below, we choose the formulation of Teixeira and Cheinet (2004):

$$l_{1D} = \tau e^{1/2}, \tag{16}$$

where τ is an eddy turnover time scale that can either be a constant or depend on parameters of the flow and e denotes the SGS turbulent kinetic energy that grows with grid length for the gray-zone resolutions.

The calculated mixing length also needs to take into account the proximity of the surface. Typically, the mixing length in the surface layer l_S grows linearly with height but may also depend upon stratification (Monin and Obukhov 1954; Mellor and Yamada 1974; Nakanishi 2001). The transition between the surface layer and the well-mixed boundary layer aloft can be achieved by merging the two scales following Blackadar (1962):

$$\frac{1}{l} = \frac{1}{l_S} + \frac{1}{l_{BL}}, \tag{17}$$

where $l_{BL} \in \{l_{1D}, l_{3D}\}$. Consequently, the mixing length smoothly changes from the surface-layer limit toward the boundary layer limit, which qualitatively describes the growth of boundary layer eddies with the distance from the ground.

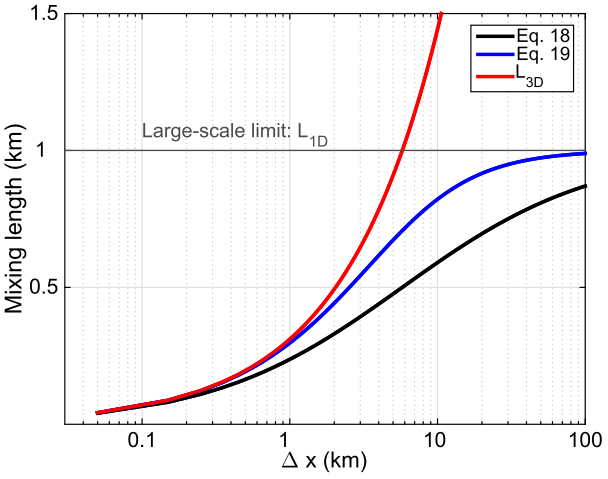

FIG. 1. A blended mixing length as a function of horizontal resolution Δx as described by Eqs. (18) (blue) and (19) (black) for a large-scale limit l_{1D} of 1 km. The geometric l_{3D} mixing length is also plotted (red).

We propose to follow this framework to merge the two asymptotic (i.e., fine and coarse) filter-scale limits:

$$\frac{1}{l_{BL}} = \frac{1}{l_{3D}} + \frac{1}{l_{1D}}. \tag{18}$$

In this simple approach, the small-scale 3D mixing length increases with the horizontal grid length until the large-scale 1D limit is reached. Further increase of the grid spacing should only have a minor impact on l_{BL}, which then becomes almost entirely dependent on boundary layer properties typical of one-dimensional models. In other words, the mixing length continuously transitions between the high-resolution l_{3D} and the coarse-resolution l_{1D} limits for different grid lengths.

To increase the convergence of l_{BL} to its asymptotic limits, Eq. (18) is modified to

$$\left(\frac{1}{l_{BL}}\right)^2 = \left(\frac{1}{l_{3D}}\right)^2 + \left(\frac{1}{l_{1D}}\right)^2, \tag{19}$$

which helps to enhance the role of l_{3D} and l_{1D} at finer and coarser resolutions, respectively, as shown in Fig. 1. This figure also exemplifies how the resulting mixing length transitions from the finescale to large-scale limits [using either Eq. (18) or (19)].

The reason behind choosing the Teixeira and Cheinet (2004) formulation for l_{1D} is twofold. First, it scales with the subgrid turbulent kinetic energy, which saturates as the resolved part diminishes. Second, it provides a natural length-scale reduction above the well-mixed boundary layer because of a significant turbulent

kinetic energy decrease in stably stratified layers. Consequently, there is no need to use a mixing-length reduction such as the one from Deardorff (1980) for stably stratified layers. The Teixeira and Cheinet (2004) formulation naturally helps to avoid arbitrary modifications of the mixing length around the boundary layer top. The Teixeira and Cheinet (2004) formulation has been implemented and evaluated in the U.S. Navy Coupled Ocean–Atmosphere Mesoscale Prediction System (Teixeira et al. 2004), has been extended to moist convective boundary layers (Cheinet and Teixeira 2003), and is at the core of the simplified higher-order closure (SHOC) methodology (Bogenschutz and Krueger 2013) and of the latest versions of the eddy diffusivity/mass flux (EDMF) approach (Suselj et al. 2012, 2013).

The mixing length in the surface layer is here defined as

$$l_S = \kappa z\, e^{z/l_0}, \tag{20}$$

where l_0 is a constant parameter. The formulation is subsequently merged with the boundary layer mixing length following Eqs. (17) and (19). This formulation is effectively similar to the approach proposed in Teixeira and Cheinet (2004), although it has two important improvements: the mixing length monotonically increases with height also for small values of l_{BL} (typical for $l_{3\mathrm{D}}$), and the depth of the surface layer does not strongly depend on the l_{BL} mixing length, remaining in the limit of around 10% of the boundary layer height also for its large values from the 1D limit. To obtain similar vertical distributions of temperature near the surface for the 3D and 1D limits for a range of mixing lengths, we use $l_0 = 60$ m.

The final form of the proposed mixing length that merges the 1D and 3D limits and the surface layer is given by

$$\left(\frac{1}{l}\right)^2 = \left(\frac{1}{l_{3\mathrm{D}}}\right)^2 + \left(\frac{1}{l_{1\mathrm{D}}}\right)^2 + \left(\frac{1}{l_S}\right)^2, \tag{21}$$

and the blended mixing length is designed such that its values are always lesser than the *smallest* of the three components. Consequently, it is controlled by l_S near the surface and by the reduced $l_{1\mathrm{D}}$ for stable stratifications. Apart from the surface and stable layers, the choice between $l_{3\mathrm{D}}$ and $l_{1\mathrm{D}}$ is dictated by the scale of the problem. In particular, for a deep boundary layer resolved at fine resolution (i.e., for $l_{3\mathrm{D}} \ll l_{1\mathrm{D}}$), l is close to $l_{3\mathrm{D}}$, which naturally relates it to the grid-size length scale, whereas for a shallow boundary layer resolved at coarse resolution (i.e., for $l_{3\mathrm{D}} \gg l_{1\mathrm{D}}$), it is close to $l_{1\mathrm{D}}$, which is associated with the boundary layer eddy scale.

TABLE 1. Typical values for the SGS model coefficients as used in the simulations of convective boundary layer by different LES models (with Δx describing their horizontal grid length) and by 1D models.

Reference	C_k	Pr	C_ϵ	Δx (m)
Klemp and Wilhelmson (1978)	0.2	0.33	0.2	1000
Deardorff (1980)	0.1	0.33	0.7	125
Moeng and Wyngaard (1988)	0.1	0.33	0.93	50
Schmidt and Schumann (1989)	0.12	0.42	0.93	50
Teixeira and Cheinet (2004)	0.5	0.33	0.4	—
Witek et al. (2011b)	0.25	0.33	0.6	—

3. Numerical experiment

a. The modeling framework

The Weather Research and Forecasting (WRF) Model is used as a framework for the multiscale simulations of the dry convective boundary layer. We employ the model configuration suitable for running idealized LES experiments (WRF-LES) in a nonhydrostatic regime, with a standard set of parameters defining the model's dynamics. A detailed description of the WRF Model, including the fully compressible governing equations and the numerical methods used for solving them, can be found in Skamarock et al. (2008) and references therein.

b. Setup of the experiment

The numerical experiment we perform to test our approach follows Siebesma et al. (2007). We therefore simulate six different surface buoyancy-driven cases (cf. Table 1 therein), which include three different stratifications, 1.95, 2.93, and 3.90 K m^{-1}, and two different values of the surface fluxes, 0.06 and 0.03 K m s^{-1}. Surface temperature and pressure are 297.2 K and 1000 hPa, respectively. The positively stratified dry atmosphere is initially at rest, and there is no external flow. The domain top is at 3 km, with a sponge layer extending above 2.6 km. The horizontal domain size changes with resolution while the number of grid points (96^3) remains fixed. The mean results are practically independent of the domain size as long as it is at least an order of magnitude larger than the boundary layer height (not shown). In the absence of large-scale flow, the varying domain size does not significantly affect the mean profiles yet facilitates the experiment and allows us to calculate the statistics over the same number of grid points regardless of grid length. The vertical grid spacing changes from around 28 m near the surface to around 36 m near the top. Periodic lateral boundary conditions are applied. The default numerical stability limiters for

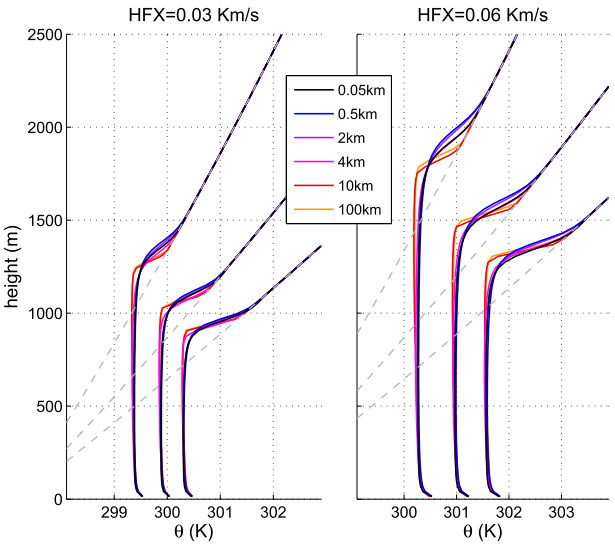

FIG. 2. Mean potential temperature profiles at the end of simulation time (10 h) for two values of surface fluxes (as indicated by HFX) and three different stratifications for simulations using six different horizontal resolutions (from 50 m to 100 km). Initial profiles for the three stratifications are plotted with gray dashed lines.

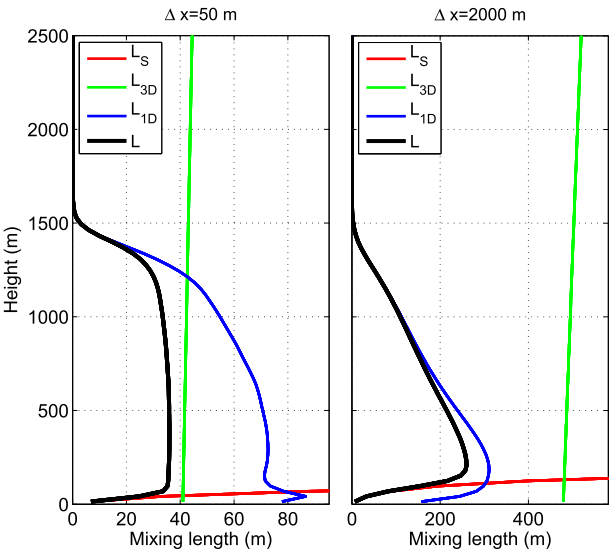

FIG. 3. Blended mixing length (black) from Eq. (21) as a function of height for the case of $\Gamma = 1.95\,\mathrm{K\,m\,s^{-1}}$ and $\mathrm{HFX} = 0.03\,\mathrm{K\,m\,s^{-1}}$ for Δx = (left) 50 m and (right) 2 km. The three generic components of the length scale (i.e., for the surface layer and 3D and 1D modes) are also plotted.

the turbulent mixing coefficients (that depend on the $\Delta z^2/\Delta t$ ratio) are switched off. The integration time is 10 h. Since a number of different options for the SGS coefficients exists in the literature (see Table 1), with generally lower values of the transport-related coefficients C_k and higher values of the energy-dissipation-rate-related coefficients C_ϵ at finer resolutions, we use a set of constants typical for LES: $C_k = 0.2$, $C_\epsilon = 0.93$, and $\mathrm{Pr} = 0.33$. The eddy turnover time τ from Eq. (16) is fixed at 1000 s.

Our main strategy is to perform a series of simulations starting from the LES limit, which always provides a reference solution, and gradually decrease the horizontal resolution down to 100 km. We then analyze the main features of such a transition and the behavior of the SGS scheme itself.

4. Testing the approach

a. Mean potential temperature

The multiresolution results for the proposed mixing-length formulation [Eq. (21)] at the end of the simulations are shown in Fig. 2. We purposely plot the potential temperature profiles in real (instead of nondimensional) height in order to highlight the differences between the simulations. In this experiment, the only scale-dependent parameter of the SGS scheme is the mixing length.

The comparison documents a similar development of the convective boundary layer for all the resolutions tested. A good agreement is observed in terms of the distribution of potential temperature within the surface and well-mixed layers, with the differences appearing mostly around the boundary layer top.

The spread of the boundary layer heights reaches approximately 80–150 m [around 5%–7% in terms of z/z_i; z_i is calculated as the height of minimum heat flux (HFX)] with somewhat larger differences for the larger value of heat flux. Only for the most active convective case (i.e., for $\overline{w'\theta'}_s = 0.06\,\mathrm{K\,m\,s^{-1}}$ and $\Gamma = 1.95\,\mathrm{K\,km^{-1}}$) does the spread reach 10%. Two different types of profiles can be distinguished depending on grid length. For finer resolutions, the profiles near the inversion are smoother as the model explicitly resolves at least part of the transport by convective plumes across the inversion. For coarser resolutions (mostly for Δx=10 and 100 km), this part of the transport diminishes along with diminishing resolved vertical velocity perturbations, which preserves the sharpness of the inversion. The transport across the inversion layer is also slightly weaker for smaller stratifications, which results from insufficient local transport of heat in the upper part of the boundary layer for faster-growing PBLs.

In Fig. 3, we plot the simulated blended mixing length for the case with the smaller surface flux and weakest stratification for the resolutions of 50 m and

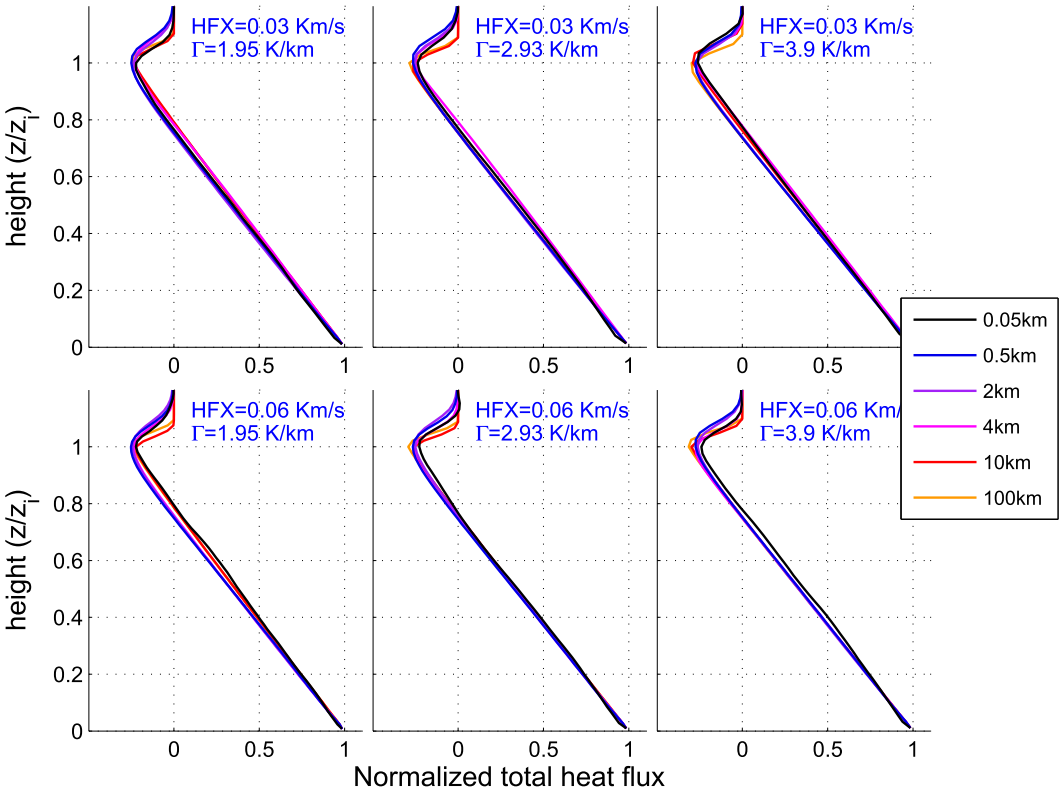

FIG. 4. Profiles of the vertical fluxes of potential temperature for the six different cases at the end of simulation time (10 h) for simulations using six different horizontal resolutions (from 50 m to 100 km). All the profiles are normalized by their surface values (HFX) and plotted using normalized height coordinates z/z_i. The potential temperature lapse rates are indicated by Γ.

2 km to illustrate how the blended mixing length is obtained using the three mixing lengths from Eq. (21). For the 50-m resolution, the blended mixing length is close to l_{3D} within the mixed layer but converges to l_S and l_{1D} in the surface and stable layers, respectively. For the 2-km resolution, the blended mixing length within the mixed layer is close to l_{1D}, with the same limits for the surface and stable layers.

b. *Vertical heat flux*

Figure 4 shows profiles of the total heat flux averaged over the last hour to reduce their temporal variability. The profiles also compare well among the resolutions. The most typical differences within the boundary layer are small and primarily concern the region around the inversion. The maximum negative buoyancy flux usually varies between 25% and 35% of the surface value, with the ensemble maxima for grid lengths around 2–4 km, and occasionally 100 km as well. These correlate well with the previously described differences regarding the potential temperature profiles and their spread at the PBL top.

Partitioning between the resolved and subgrid-scale transports is shown in Figs. 5 and 6, in which mean profiles of the two types of vertical transport are plotted. For the finest resolution, the subgrid-scale contribution is only important near the lower and upper boundaries of the convective layer, where it controls the surface fluxes and slightly affects the entrainment across the inversion, respectively. As the grid length increases, the subgrid-scale transport penetrates deeper into the layer above the surface at the cost of a less efficient explicit transport by rising thermals. At the same time, its maximum near the top of the layer gradually increases, and the zone of its influence deepens downward. For Δx of about 8–10 km, the resolved part becomes only a few-percent residual of the total transport.

Another way of looking at the transition is to analyze the partitioning between the SGS and the resolved heat flux across resolutions. Figure 7 shows both contributions, normalized by the total values, as a function of the nondimensional resolution $\Delta x/z_i$ from the last simulation hour, for the positive part of the total flux

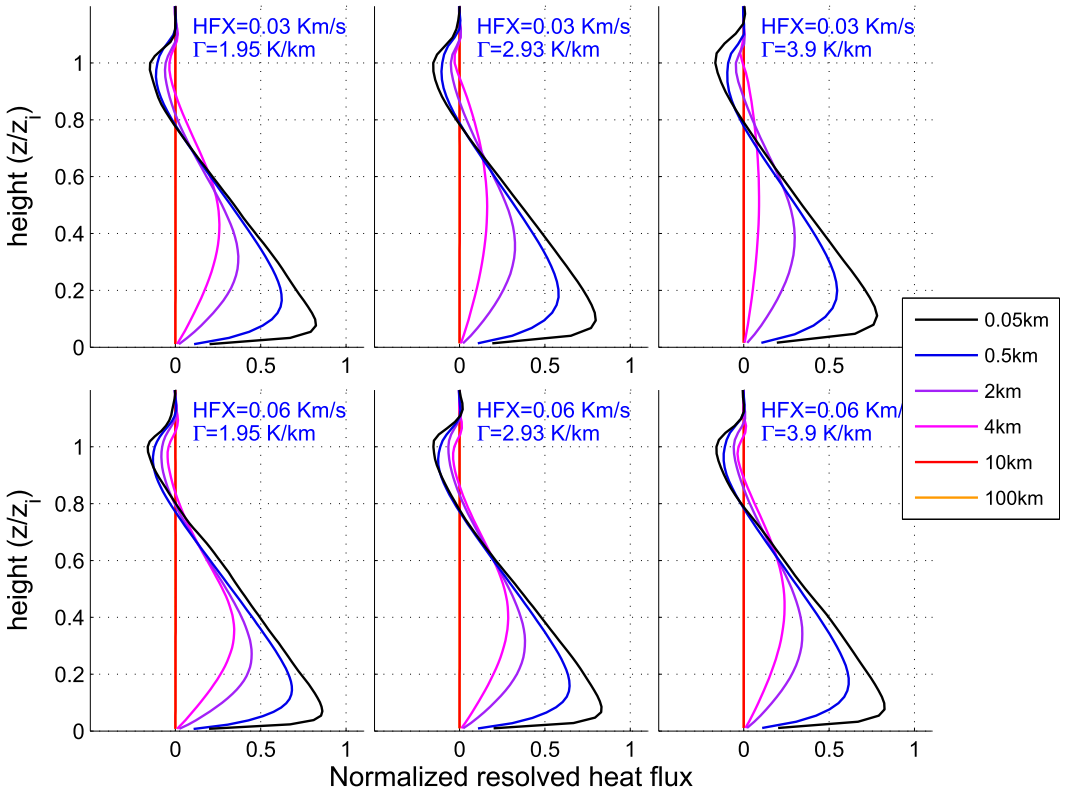

FIG. 5. As in Fig. 4, but for the resolved part of the heat flux.

(between 0.1 and $0.5z/z_i$). Two additional simulations using $\Delta x = 200$ m and 2 km have been performed for each of the six cases to fill out the gaps between the six originally tested resolutions. The general picture of the transition is similar to that previously obtained from filtered high-resolution LES results (Honnert et al. 2011; Shin and Hong 2013). A number of simulated cases with different surface conditions and stratifications yield a spread in the results, contributing to the uncertainty of the partitioning for a given resolution. For instance, equal partitioning between the two parts occurs for values of $\Delta x/z_i$ between approximately 0.5 and 3, with the ensemble mean around 1.9. The greater values are generally associated with more vigorous convective cases. These values characterize the behavior of the local SGS scheme and are larger than for the partitioning from Honnert et al. (2011), which was around 0.4. A full transition to the subgrid-scale transport occurs for $\Delta x/z_i$ between 6 and 7, which is also somewhat larger than in Honnert et al. (2011). Similar differences in the SGS transport between the simulated and coarse-grained results were also reported by Kitamura (2016) for their TKE-based LES model or by Efstathiou and Beare (2015) for their Smagorinsky-type model. Efstathiou and Beare (2015) associated them with the numerical effects that are not present in coarse-grained LES results.

c. *Turbulent kinetic energy*

The largest differences among the resolutions appear for total TKE (Fig. 8). The total TKE is calculated as a sum of the subgrid-scale and the resolved parts (Sullivan and Patton 2011). Its value is subsequently normalized by the squared product of the convective velocity scale:

$$w_* = \left[\frac{g}{T_s}\overline{(w'\theta')}_s z_i\right]^{1/3}, \tag{22}$$

where the subscript s refers to the surface and z_i denotes the boundary layer height (different for each simulation).

The results from Fig. 8 are not surprising since typical distributions of TKE have different characteristics for the small- and large-scale limits. For the former, it is relatively uniform across the boundary layer depth (e.g., Sullivan and Patton 2011). For the latter, however, it is usually proportional to the square root of the subgrid-scale convective velocity scale that has a distinct

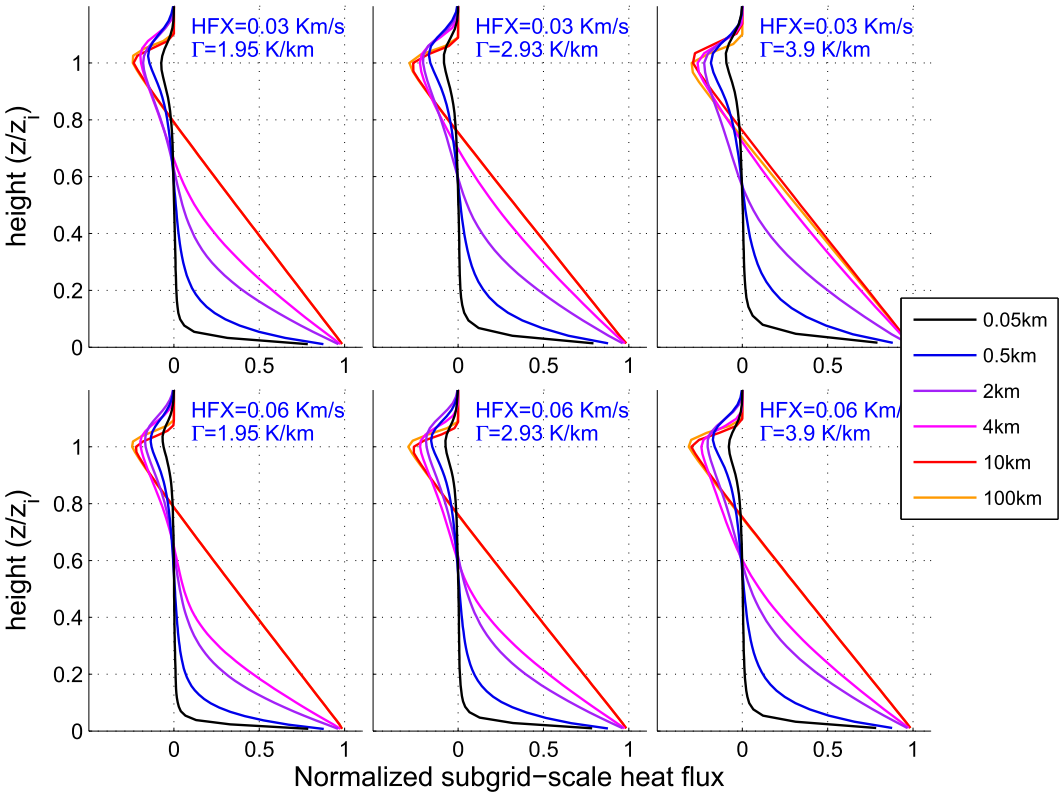

FIG. 6. As in Fig. 4, but for the subgrid-scale part of the heat flux.

midlayer maximum (cf. Teixeira and Cheinet 2004; Witek et al. 2011b). These differences indicate the shortcomings of the low-resolution representation since both profiles should be consistent.

A similar behavior is also observed in the current experiment. The total TKE, which is relatively equally distributed with height for the finest meshes, gradually decreases in the upper part of the boundary layer at coarser grid lengths. For the largest grid lengths, TKE near the inversion drops to almost zero. At the same time, TKE tends to accumulate in the lower part of the boundary layer because of the lack of nonlocal SGS transport by convective coherent structures. This transport becomes increasingly important for poorly resolved flows as the local transport is not able to provide enough vertical mixing already for Δx larger than around 1 km. Witek et al. (2011a) showed that the issue can be improved by introducing an additional nonlocal transport term in the TKE prognostic equation.

The vertically integrated amount of total TKE tends to decrease with grid length for intermediate Δx, reaching a minimum around 10 km, and then only minimally increases. Such a decrease is the result of a gradually diminishing model-resolved TKE, which is not entirely fulfilled with the SGS part. The latter increases with a growing mixing length that reduces the energy dissipation rate. This increase can be seen at coarse resolutions, when the model-resolved contribution becomes negligible. Note that in our experiment, C_ϵ remains constant across the range of Δx, although its values for the two asymptotic limits (1D and 3D) typically differ by a factor of 2 or so (cf. Table 1).

Figure 9 shows the partitioning between the resolved and SGS parts of TKE within most of the boundary layer (i.e., for $0.05 < z/z_i < 0.85$). The transition is similar to that for the vertical heat flux; however, the variability among the simulated cases is now significantly smaller. The spread among different simulations leads to equal partitioning for $\Delta x/z_i$ ranging from around 1.1 to 3, with the mean value around 2. Overall, the behavior of the simulated heat flux and TKE partitionings across the resolutions tends to be shifted toward larger $\Delta x/z_i$ when compared to Honnert et al. (2011), which can be considered the reference dataset to evaluate our results, although the latter were obtained by coarse graining the LES results rather than explicitly simulating the flow for different resolutions. Note that Honnert et al. (2011) indicates that the shift toward larger $\Delta x/z_i$ is associated with closures that utilize eddy-diffusivity (ED) approaches

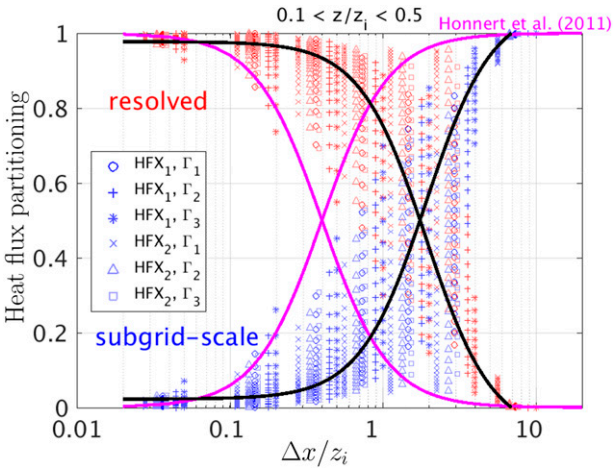

FIG. 7. Partitioning between the SGS and the resolved heat fluxes as a function of dimensionless resolution $\Delta x/z_i$ from the last simulation hour for $0.1 < z/z_i < 0.5$. Each point represents a value from the mean profiles from Figs. 4 and 5. Each simulated case is represented by a pair of corresponding red (resolved) and blue (SGS) sets of markers. Two different values of HFX and three different stratifications Γ are considered, as shown in the legend for the subgrid-scale part, with greater values of both associated with larger subscript numbers. The smoothed ensemble means are plotted with black lines. Reference partitioning from a coarse-grained LES (Honnert et al. 2011) is plotted in magenta.

(such as the one proposed here), while the opposite (the shift toward smaller $\Delta x/z_i$) is associated with nonlocal closures (e.g., when a mass-flux term is included).

d. TKE source and sink terms

To analyze the contributions from the different source terms in the TKE equation, Fig. 10 presents mean profiles of the subgrid-scale forcings due to shear, buoyancy, transport, and dissipation for a range of horizontal grid lengths. The mean advection term oscillates around zero and is excluded from the analysis. The TKE source and sink terms are first normalized by w_*^3/z_i and interpolated vertically into a nondimensional space z/z_i and then averaged over the six cases. In addition to mean profiles, shaded areas representing one standard deviation are plotted.

For the finest grid length, the most significant contributions within the boundary layer are the shear production by explicitly resolved local circulations, which is counterbalanced by dissipation. Additionally, a local contribution from the surface buoyancy production can be noted. These two sources (i.e., shear or buoyancy) describe the two ways turbulence can be produced by the SGS model. The shear production gradually diminishes as local velocity gradients diminish at coarser grid lengths, although it is still notable (i.e., 20%–30% of the finest-resolution values) for 2–4-km grid lengths. The buoyancy production increases with grid length: the thickness of a layer for which this source term is positive increases with grid length from $0.1z/z_i$ (for $\Delta x = 50$ m) to around $0.8z/z_i$ (for $\Delta x \geq 10$ km). The mean turbulent transport term is negative within most of the boundary layer except for the surface and inversion layers. This is due to the fact that, for quasi-steady state, maximum TKE occurs above the surface layer. Since the SGS transport term acts to reduce local gradients, it means that the source term will be positive in the regions of TKE deficit. The dissipation rate is proportional to the amount of TKE (and inversely proportional to the mixing length), and therefore, it has the largest values near the ground that decrease with height. The profiles for the 10-km grid length are almost the same as for 100 km, documenting a complete transition to the virtually one-dimensional regime with no shear production and buoyancy production linearly decreasing with height. Because the mixing length still grows in this limit, the energy dissipation rate for larger grid lengths further decreases. As a result, the total amount of TKE within the boundary layer (as well as the entrainment rate) also increases (cf. Fig. 8).

The variability of the source terms as measured by their standard deviations is relatively small for grid lengths not exceeding 0.5 km. For the large-scale limit, the mean profiles already stabilize at $\Delta x = 10$ km. The most critical resolutions seem to be around $\Delta x = 4$ km, for which most of the forcings reveal the largest case-to-case fluctuations. For less vigorous convection, the SGS scheme already behaves as within the large-scale limit. For stronger surface forcings and/or weaker vertical stability, the scheme tends to reveal more finescale features, including the reduced contributions from the SGS buoyancy and transport terms.

e. Comparison with a TKE-based LES model using only a geometric mixing length

The original TKE-based LES model developed by Deardorff (1980) was designed to fully resolve fluid flow at scales larger than the LES grid size (a few tens of meters) and to utilize the TKE closure to parameterize the subgrid turbulent mixing. In that model, the mixing length explicitly depends on the LES grid size (a geometric mixing length, as in l_{3D}). LES models such as Deardorff (1980) are generally not designed to be able to realistically represent turbulent and convective mixing (either explicitly or in parameterized form) when using grid sizes that are much larger than typical LES grid sizes. In any case, in here, we test the ability of a TKE-based LES model (using a geometric mixing length) to represent the dry convective boundary layers that are simulated in this paper, with grid sizes ranging

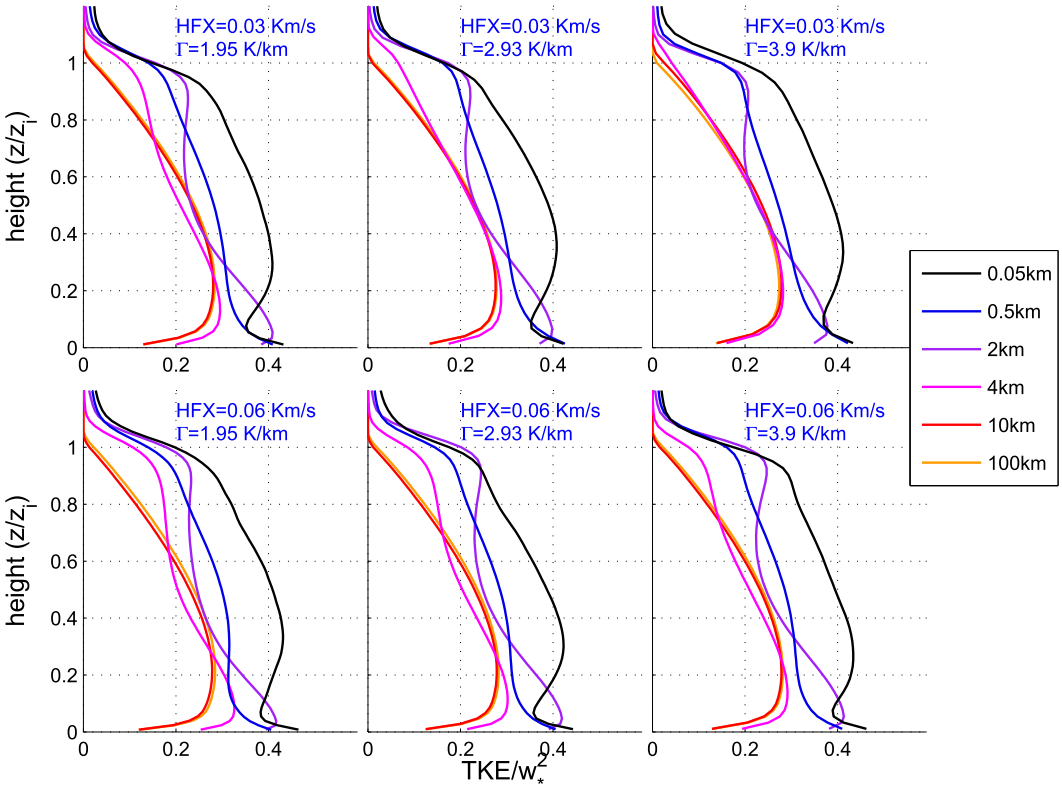

FIG. 8. Normalized profiles of the total TKE at the end of the simulations for different horizontal grid lengths and for the six simulated cases.

from 50 m to 100 km. We compare the new approach against a TKE-based LES model to assess the role of the key elements of the new mixing length: (i) the merging of the 1D and 3D mixing-length limits, (ii) the 1D mixing length that naturally decreases in stable layers (leading to a smooth transition close to the boundary layer top and, as such, impacting the top entrainment), and (iii) the modified surface-layer mixing length.

It should be stressed, however, that there are different versions of TKE-based LES models—even among the ones more strictly following Deardorff (1980). A key common element for these models is the geometric mixing length [Eq. (15)]. Other features (e.g., the Prandtl number or the mixing length in stable layers) are less strictly followed. It turns out that these additional elements may significantly affect the results, as briefly described below. Moreover, the original work of Deardorff (1980) neglects the mixing-length modifications in the surface layer, which are increasingly important at coarser resolutions.

Simulations with a TKE-based LES model for horizontal resolutions from 50 m to 100 km were performed for different versions of the LES model (all these versions used the geometric mixing length mentioned above): with and without the mixing-length stability correction (e.g., Deardorff 1980) and with and without a surface-layer mixing length. Note that, in all simulations, the numerical stability limiters for the turbulent mixing coefficients were switched off.

All the simulations show that the TKE-based LES model using only a geometric mixing length (proportional to the LES 3D grid size) produces a development of the dry convective boundary layer that is similar to the one produced by the formulation proposed in this paper for resolutions typical of LES (i.e., 50 m and slightly larger). This is an expected result, since the new scale-adaptive mixing length converges to the LES geometric mixing length for these high resolutions—although the surface-layer mixing length can play a significant role even at these resolutions.

For coarser resolutions (mostly for resolutions above 4 km), the simulations with the TKE-based LES using a geometric mixing length only show an unrealistically large growth of the dry convective boundary layer. This is essentially due to the extremely large values of the geometric mixing length for low resolutions, which leads to large values of the eddy-diffusivity coefficient and an

anomalous transition from the convective boundary layer to the stable atmosphere above. Note that for a horizontal resolution of 100 km, the geometric mixing length is around 10 km (clearly much larger than the boundary layer depth).

This is illustrated well in Fig. 11, where the ED coefficients for the different resolutions and two different formulations are shown: (i) the scale-adaptive formulation proposed in this paper and (ii) the basic TKE-based LES model with a purely geometric mixing-length formulation (both models use the same surface-layer mixing length—otherwise, the basic LES model's results are even less realistic). It can be seen that the ED coefficients start to differ between the two models for resolutions of 500 m and above, with these differences becoming larger and larger at coarser resolutions. The ED coefficients for the new method proposed here converge to a value determined by the boundary layer height scale (from l_{1D}) as the grid size increases, while the growth of the ED coefficients for the basic LES version follows the growth of the geometric mixing length with grid size, reaching a peak value close to 2000 $m^2 s^{-1}$ for a resolution of 100 km. Values of this nature for the mixing length and ED coefficient lead not only to unrealistic dry convective boundary layers but would also potentially play a damaging role in the overall simulations if other parameterizations and processes (e.g., moist convection, cloud condensation, and microphysics) were to be coupled to the ED parameterization of dry turbulent/convective mixing.

f. Horizontal subgrid transport

The final element we inspect in this study is the horizontal subgrid flux defined as

$$\overline{u'\theta'} = -K_h \frac{\partial \overline{\theta}}{\partial x} \tag{23}$$

and

$$\overline{v'\theta'} = -K_h \frac{\partial \overline{\theta}}{\partial y} \tag{24}$$

in the two horizontal directions.

In Fig. 12, the ensemble mean of absolute subgrid horizontal fluxes for $0.1 < z/z_i < 0.5$ is shown as a function of horizontal resolution. For reference, we also plot the vertical subgrid flux. The averaging procedure uses the fluxes normalized by the surface values and neglects their direction. As expected, the vertical heat flux changes from around 10^{-2} to 0.5 as the flow transitions from 3D to 1D (cf. Fig. 6). However, the behavior of the horizontal component is less obvious. Starting from the finest grid length, it slightly grows (on logarithmic scale) to reach the maximum for the 0.5–1-km grid lengths and then slightly decreases. Above $\Delta x = 4$ km, it drops abruptly, and then the negative trend remains for the larger grid lengths as well. One can therefore distinguish two regimes for the horizontal fluxes. At finer resolutions, when the flow is at least partially resolved, they are fairly similar regardless of grid length. Once the transition to 1D mode completes, it begins decreasing with grid length. Similarly, two regimes also appear for the vertical fluxes with a steady growth until about 10 km and a constant value at coarser resolutions.

Since the horizontal subgrid flux is defined as the product of the eddy-diffusivity coefficient and the potential temperature gradient, we examine the mean behavior of the two components across resolutions.[1] As was shown in Fig. 11, the mean turbulent mixing coefficient constantly grows, with grid length reaching its asymptotic value around $\Delta x = 10$ km. On the other hand, the mean horizontal temperature gradient decreases with grid length but at a lower rate for finer resolutions. This slow decrease in the gradient is counterbalanced by the increase in the mixing coefficient, which turns out to be sufficient for maintaining similar horizontal fluxes between $\Delta x = 50$ m and 4 km. For the larger rate decrease (at coarser resolutions), the eddy-diffusivity coefficient stops growing, and the flux follows the temperature gradient decrease.

It is also insightful to compare mean absolute potential temperature differences as a function of grid length (Fig. 13). They constantly grow with grid length up to $\Delta x = 4$ km and then abruptly drop by more than an order of magnitude. This finer-scale increase is largely caused by the disintegration of convective cells and a relative increase in the amount of grids with the temperature excess since the maximum temperature differences (also plotted in the figure) only slightly grow with grid length. In the large-scale limit, the mean and maximum potential temperature differences are at least an order of magnitude smaller and show only minimal fluctuations among the model grid points. The significant drop in the temperature differences between 4 and 10 km is due to the fact that, at 10 km, the model is incapable of producing any type of

[1] Although averaging of the product of two elements is in general not equivalent to the product of two averaged elements, we look into them to get a hint on the nature of the scale dependence from Fig. 12.

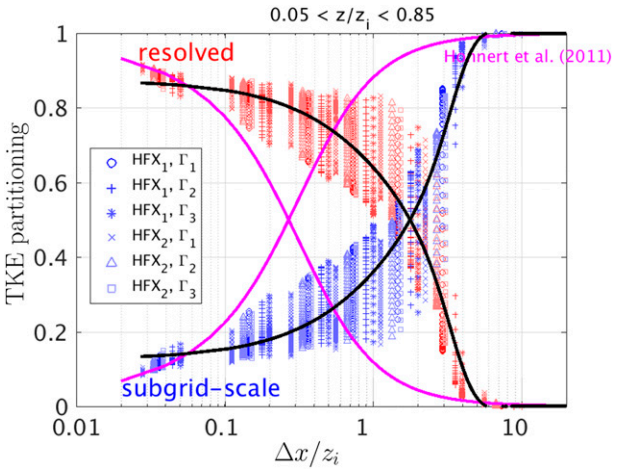

FIG. 9. As in Fig. 7, but for TKE. A reference solution from a coarse-grained LES (Honnert et al. 2011) is plotted in magenta.

convective structures (even numerically spurious ones), which leads to extremely small horizontal temperature perturbations.

5. Summary and discussion

In this paper, a scale-adaptive turbulent kinetic energy (TKE) closure for the dry convective boundary layer is proposed. Since the TKE closure has been widely used in high-resolution LES models (in 3D mode) and in coarse-resolution weather and climate prediction models (in 1D mode), we use a simple method to merge in a continuous manner these two distinct limits across intermediate resolutions. A mixing-length formulation is proposed that is inspired by the Blackadar (1962) formulation to merge the surface layer with the boundary layer mixing length.

The new scale-adaptive mixing length continuously increases with an increasing grid length for intermediate resolutions and naturally saturates close to the boundary layer length scale. It is shown that the proposed mixing-length formulation leads to a natural and continuous transition of the subgrid-scale vertical transport for a wide range of horizontal grid lengths, including the turbulent gray zone, although there is

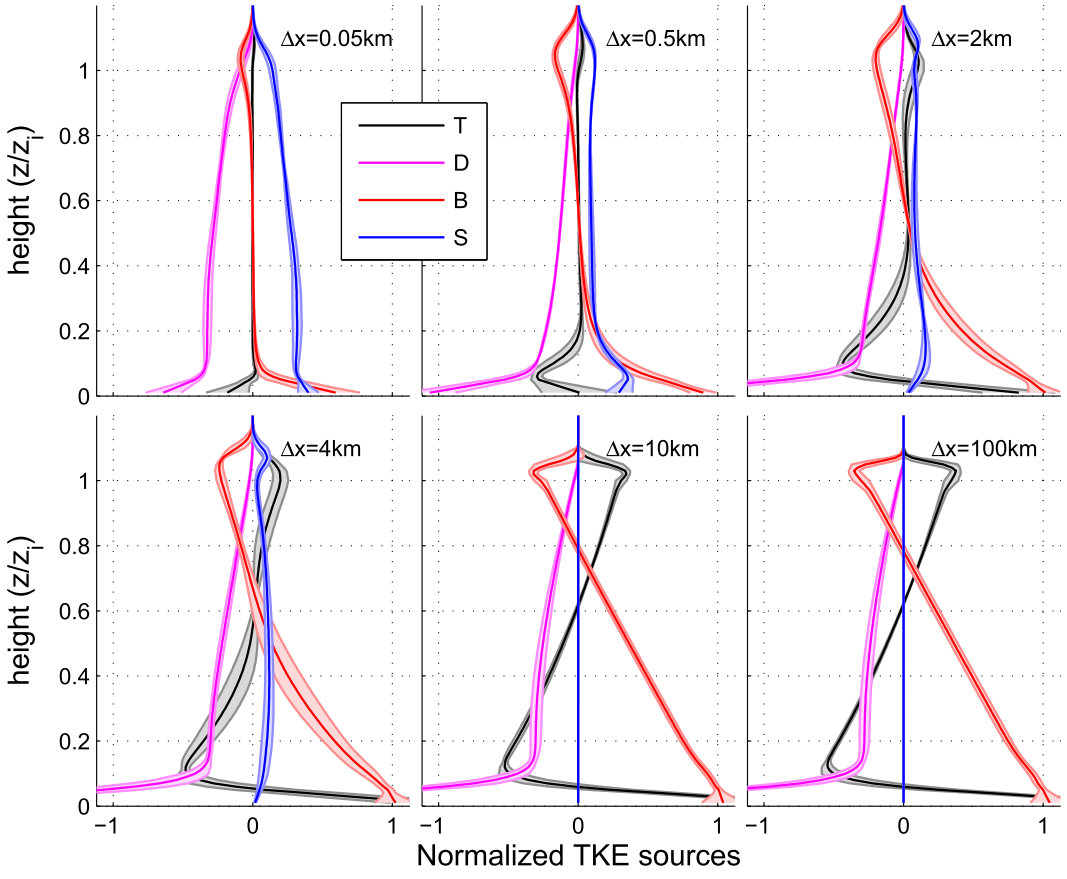

FIG. 10. Normalized horizontally averaged profiles of the subgrid-scale TKE source and sink terms (transport T, dissipation D, buoyancy B, and shear S) for a range of horizontal resolutions as indicated by Δx. The ensemble means (thick lines) are plotted together with the envelopes of one standard deviation (lighter colors).

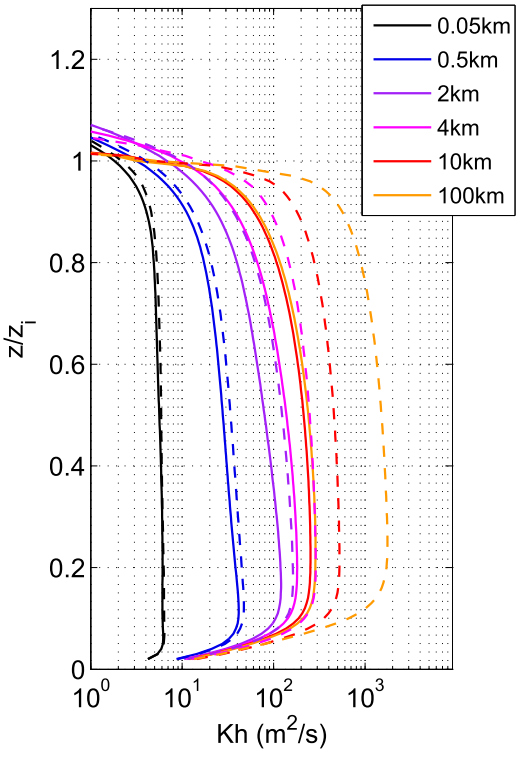

FIG. 11. Ensemble-mean vertical profiles of horizontally averaged turbulent mixing coefficients for heat from the simulations with the new model (continuous lines) and the Deardorff (1980) model (dashed lines) at the end of the simulation time. Both models employ the same surface-layer mixing-length formulation.

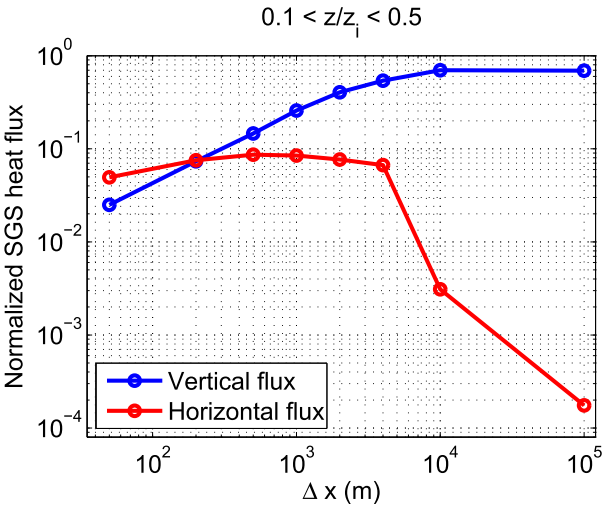

FIG. 12. Horizontally averaged subgrid vertical and horizontal fluxes for $0.1 < z/z_i < 0.5$ normalized by the surface heat flux. Absolute values of the local horizontal flux are considered to emphasize the magnitude of heat flow also in the horizontal. Each line represents the ensemble mean over the six convective cases.

still room for improvement at these intermediate resolutions.

The new mixing-length approach is tested for a variety of cases of dry convection forced by a constant surface buoyancy flux: six different cases with two different surface fluxes and three different stratifications are considered. Each of the cases includes simulations for horizontal grid resolutions spanning three orders of magnitude, from 50 m to 100 km. The simulation results document a similar development of the boundary layer in terms of the mean potential temperature profiles for all the resolutions tested, although sharper temperature inversions are obtained for coarser resolutions. The profiles of total heat flux compare well among the resolutions. It is clear (as it has been shown in other studies referenced in the paper) that a pure eddy-diffusivity (ED) approach in 1D will not produce a fully realistic depiction of the structure of the boundary layer (i.e., a well-mixed layer) and that an additional term is required to represent the countergradient fluxes. Such a term, like a mass-flux (MF) parameterization of convective plumes (as in EDMF; e.g., Siebesma et al. 2007) is necessary and should be scale adaptive as well. In the current paper, we opted for utilizing an ED closure, without accounting for a countergradient term, to test, in the simplest manner possible, the mixing-length formulation that blends the traditional TKE LES and 1D closures.

The partitioning between the resolved and subgrid components of the heat flux and turbulent kinetic energy, for different resolutions, follows the expected qualitative behavior similar to Honnert et al. (2011): with the fluxes (TKE) being mostly resolved at higher resolutions, transitioning in a continuous manner to dominant subgrid fluxes (TKE) at lower resolutions. However, there are still differences when compared to Honnert et al. (2011); for example, the normalized grid length at which equal partitioning occurs is greater. Although it should be noted that their results are essentially diagnostic and are obtained by spatial filtering of LES for different filter scales. They do not explicitly simulate the atmosphere using the same model for a variety of grid resolutions as it is done in the study presented here.

It can be argued that the most remarkable results from the current paper pertain to the simulation of the different source and sink terms of the prognostic TKE equation. Our simulations show a natural and continuous transition from a situation where the shear production and dissipation dominate (for 50-m resolution) to a situation dominated by the buoyancy production, dissipation, and transport of TKE (for 100-km resolution).

The comparison with a basic TKE-based LES model (with just a geometric mixing length) illustrates the

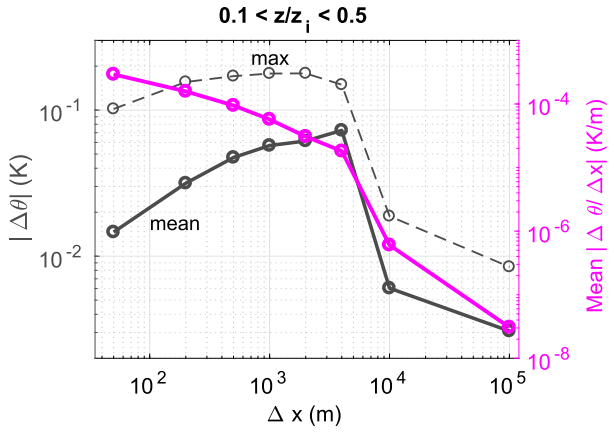

FIG. 13. Mean and maximum absolute values of the horizontal potential temperature differences and the horizontal potential temperature gradients for $0.1 < z/z_i < 0.5$ from the ensemble of convective cases.

advantages of the new approach by highlighting the issues faced by the basic LES, which include an unrealistic growth of the boundary layer and extremely large values for the mixing-length and eddy-diffusivity coefficients for coarse resolutions.

For completeness, we also analyze how scale adaptive the horizontal subgrid temperature fluxes are. For grid sizes between 50 m and 4 km, they remain comparable, reaching a maximum around 0.5–1 km. Between 4 and 10 km, the horizontal subgrid fluxes decrease dramatically by more than one order of magnitude. This significant drop is essentially because, at 10 km, the model is no longer capable of producing any type of convective structures (even numerically spurious ones), which leads to extremely small horizontal temperature perturbations. Overall, the horizontal subgrid fluxes decrease by almost three orders of magnitude from a resolution of 50 m to a resolution of 100 km.

In this paper, it is shown that by using the exact same atmospheric model (without changes to any parameter), it is possible to simulate in a realistic manner (without any arbitrarily imposed resolution-dependent formulation) the key properties of the dry convective boundary for horizontal grid resolutions spanning three orders of magnitude: from 50 m to 100 km. This is achieved by using a new mixing-length formulation that naturally merges in a fairly simple manner the essential mixing-length scales from LES to weather and climate models.

Future research will focus on extending the methodology to more complex convective boundary layers such as stratocumulus and cumulus boundary layers and developing scale-adaptive approaches to nonlocal turbulent and convective transport by boundary layer plumes that plays a critical role in the evolution of convective boundary layers. This will be performed in the context of recent approaches such as EDMF that aim to unify the representation of local and nonlocal boundary layer and convective mixing.

Acknowledgments. Part of this research was carried out at the Jet Propulsion Laboratory, California Institute of Technology, under a contract with the National Aeronautics and Space Administration. Part of this research was supported by the U.S. Department of Energy, Office of Biological and Environmental Research, Earth System Modeling. We also acknowledge the support provided by the NASA MAP Program and the NOAA/CPO MAPP Program. Drs. Marcin Witek and Kay Suselj are acknowledged for their comments on the manuscript.

REFERENCES

Bhattacharya, R., and B. Stevens, 2016: A two turbulence kinetic energy model as a scale-adaptive approach to modeling the planetary boundary layer. *J. Adv. Model. Earth Syst.*, **8**, 224–243, https://doi.org/10.1002/2015MS000548.

Blackadar, A. K., 1962: The vertical distribution of wind and turbulent exchange in a neutral atmosphere. *J. Phys. Res.*, **67**, 3095–3102, https://doi.org/10.1029/JZ067i008p03095.

Bogenschutz, P. A., and S. K. Krueger, 2013: A simplified PDF parameterization of subgrid-scale clouds and turbulence for cloud-resolving models. *J. Adv. Model. Earth Syst.*, **5**, 195–211, https://doi.org/10.1002/jame.20018.

Boutle, I. A., J. E. J. Eyre, and A. P. Lock, 2014: Seamless stratocumulus simulation across the turbulent gray zone. *Mon. Wea. Rev.*, **142**, 1655–1668, https://doi.org/10.1175/MWR-D-13-00229.1.

Cheinet, S., and J. Teixeira, 2003: A simple formulation for the eddy-diffusivity parameterization of cloud-topped boundary layers. *Geophys. Res. Lett.*, **30**, 1930, https://doi.org/10.1029/2003GL017377.

Cheng, A., K.-M. Xu, and B. Stevens, 2010: Effects of resolution on the simulation of boundary-layer clouds and the partition of kinetic energy to subgrid scales. *J. Adv. Model. Earth Syst.*, **2** (1), https://doi.org/10.3894/JAMES.2010.2.3.

Deardorff, J. W., 1980: Stratocumulus-capped mixed layer derived from a three-dimensional model. *Bound.-Layer Meteor.*, **18**, 495–527, https://doi.org/10.1007/BF00119502.

Dorrestijn, J., D. T. Crommelin, A. P. Siebesma, and H. J. J. Jonker, 2013: Stochastic parameterization of shallow cumulus convection estimated from high-resolution model data. *Theor. Comput. Fluid Dyn.*, **27**, 133–148, https://doi.org/10.1007/s00162-012-0281-y.

Efstathiou, G. A., and R. J. Beare, 2015: Quantifying and improving sub-grid diffusion in the boundary-layer grey zone. *Quart. J. Roy. Meteor. Soc.*, **141**, 3006–3017, https://doi.org/10.1002/qj.2585.

Fan, J., and Coauthors, 2015: Improving representation of convective transport for scale-aware parameterization: 1. Convection and cloud properties simulated with spectral bin and

bulk microphysics. *J. Geophys. Res. Atmos.*, **120**, 3485–3509, https://doi.org/10.1002/2014JD022142.

Grenier, H., and C. S. Bretherton, 2001: A moist PBL parameterization for large-scale models and its application to subtropical cloud-topped marine boundary layers. *Mon. Wea. Rev.*, **129**, 357–377, https://doi.org/10.1175/1520-0493(2001)129<0357:AMPPFL>2.0.CO;2.

Holloway, C. E., and Coauthors, 2014: Understanding and representing atmospheric convection across scales: Recommendations from the meeting held at Dartington Hall, Devon, UK, 28–30 January 2013. *Atmos. Sci. Lett.*, **15**, 348–353, https://doi.org/10.1002/asl2.508.

Honnert, R., 2016: Representation of the grey zone of turbulence in the atmospheric boundary layer. *Adv. Sci. Res.*, **13**, 63–67, https://doi.org/10.5194/asr-13-63-2016.

——, V. Masson, and F. Couvreux, 2011: A diagnostic for evaluating the representation of turbulence in atmospheric models at the kilometric scale. *J. Atmos. Sci.*, **68**, 3112–3131, https://doi.org/10.1175/JAS-D-11-061.1.

Ito, J., H. Niino, M. Nakanishi, and C.-H. Moeng, 2015: An extension of the Mellor–Yamada model to the terra incognita zone for dry convective mixed layers in the free convection regime. *Bound.-Layer Meteor.*, **157**, 23–43, https://doi.org/10.1007/s10546-015-0045-5.

Kitamura, K., 2016: Improving a turbulence scheme for the terra incognita in a dry convective boundary layer. *J. Meteor. Soc. Japan*, **94**, 491–506, https://doi.org/10.2151/jmsj.2016-028.

Klemp, J. B., and R. B. Wilhelmson, 1978: The simulation of three-dimensional convective storm dynamics. *J. Atmos. Sci.*, **35**, 1070–1096, https://doi.org/10.1175/1520-0469(1978)035<1070:TSOTDC>2.0.CO;2.

LeMone, M. A., M. Tewari, F. Chen, and J. Dudhia, 2013: Objectively determined fair-weather CBL depths in the ARW-WRF model and their comparison to CASES-97 observations. *Mon. Wea. Rev.*, **141**, 30–54, https://doi.org/10.1175/MWR-D-12-00106.1.

Mellor, G. L., and T. Yamada, 1974: A hierarchy of turbulence closure models for planetary boundary layers. *J. Atmos. Sci.*, **31**, 1791–1806, https://doi.org/10.1175/1520-0469(1974)031<1791:AHOTCM>2.0.CO;2.

Moeng, C.-H., and J. C. Wyngaard, 1988: Spectral analysis of large-eddy simulations of the convective boundary layer. *J. Atmos. Sci.*, **45**, 3574–3587, https://doi.org/10.1175/1520-0469(1988)045<3573:SAOLES>2.0.CO;2.

Monin, A. S., and A. M. F. Obukhov, 1954: Basic laws of turbulent mixing in the surface layer of the atmosphere. *Contrib. Geophys. Inst. Acad. Sci. USSR*, **151**, 163–187.

Nakanishi, M., 2001: Improvement of the Mellor–Yamada turbulence closure model based on large-eddy simulation data. *Bound.-Layer Meteor.*, **99**, 349–378, https://doi.org/10.1023/A:1018915827400.

Schmidt, H., and U. Schumann, 1989: Coherent structures of the convective boundary layer derived from large-eddy simulation. *J. Fluid Mech.*, **200**, 511–562, https://doi.org/10.1017/S0022112089000753.

Shin, H. H., and S.-Y. Hong, 2013: Analysis of resolved and parameterized vertical transports in convective boundary layers at gray-zone resolutions. *J. Atmos. Sci.*, **70**, 3248–3261, https://doi.org/10.1175/JAS-D-12-0290.1.

——, and ——, 2015: Representation of the subgrid-scale turbulent transport in convective boundary layers at gray-zone resolutions. *Mon. Wea. Rev.*, **143**, 250–271, https://doi.org/10.1175/MWR-D-14-00116.1.

Siebesma, P. A., P. M. M. Soares, and J. Teixeira, 2007: A combined eddy-diffusivity mass-flux approach for the convective boundary layer. *J. Atmos. Sci.*, **64**, 1230–1248, https://doi.org/10.1175/JAS3888.1.

Skamarock, W., and Coauthors, 2008: A description of the Advanced Research WRF version 3. NCAR Tech. Note NCAR/TN-475+STR, 113 pp., https://doi.org/10.5065/D68S4MVH.

Sullivan, P. P., and E. G. Patton, 2011: The effect of mesh resolution on convective boundary layer statistics and structures generated by large-eddy simulation. *J. Atmos. Sci.*, **68**, 2395–2415, https://doi.org/10.1175/JAS-D-10-05010.1.

Suselj, K., J. Teixeira, and G. Matheou, 2012: Eddy diffusivity/mass flux and shallow cumulus boundary layer: An updraft PDF multiple mass flux scheme. *J. Atmos. Sci.*, **69**, 1513–1533, https://doi.org/10.1175/JAS-D-11-090.1.

——, ——, and D. Chung, 2013: A unified model for moist convective boundary layers based on a stochastic eddy-diffusivity/mass-flux parameterization. *J. Atmos. Sci.*, **70**, 1929–1953, https://doi.org/10.1175/JAS-D-12-0106.1.

Takemi, T., and R. Rotunno, 2003: The effects of subgrid model mixing and numerical filtering in simulations of mesoscale cloud systems. *Mon. Wea. Rev.*, **131**, 2085–2101, https://doi.org/10.1175/1520-0493(2003)131<2085:TEOSMM>2.0.CO;2.

Teixeira, J., and S. Cheinet, 2004: A simple mixing length formulation for the eddy-diffusivity parameterization of dry convection. *Bound.-Layer Meteor.*, **110**, 435–453, https://doi.org/10.1023/B:BOUN.0000007230.96303.0d.

——, J. P. Ferreira, P. Miranda, T. Haack, J. Doyle, A. P. Siebesma, and R. Salgado, 2004: A new mixing-length formulation for the parameterization of dry convection: Implementation and evaluation in a mesoscale model. *Mon. Wea. Rev.*, **132**, 2698–2707, https://doi.org/10.1175/MWR2808.1.

——, and Coauthors, 2008: Parameterization of the atmospheric boundary layer: A view from just above the inversion. *Bull. Amer. Meteor. Soc.*, **89**, 453–458, https://doi.org/10.1175/BAMS-89-4-453.

Witek, M., J. Teixeira, and G. Matheou, 2011a: An eddy diffusivity–mass flux approach to the vertical transport of turbulent kinetic energy in convective boundary layers. *J. Atmos. Sci.*, **68**, 2385–2393, https://doi.org/10.1175/JAS-D-11-06.1.

——, ——, and ——, 2011b: An integrated TKE-based eddy diffusivity/mass flux boundary layer closure for the dry convective boundary layer. *J. Atmos. Sci.*, **68**, 1526–1540, https://doi.org/10.1175/2011JAS3548.1.

Wyngaard, J., 2004: Toward numerical modeling in the ''terra incognita.'' *J. Atmos. Sci.*, **61**, 1816–1826, https://doi.org/10.1175/1520-0469(2004)061<1816:TNMITT>2.0.CO;2.

Zhou, B., J. S. Simon, and F. K. Chow, 2014: The convective boundary layer in the terra incognita. *J. Atmos. Sci.*, **71**, 2545–2563, https://doi.org/10.1175/JAS-D-13-0356.1.